ACS APPLIED MATERIALS & INTERFACES
Research Article
www.acsami.org

Optimization of 1D ZnO@TiO$_2$ Core–Shell Nanostructures for Enhanced Photoelectrochemical Water Splitting under Solar Light Illumination

Simelys Hernández,*[,†] Valentina Cauda,[†] Angelica Chiodoni,[†] Stefano Dallorto,[‡,§] Adriano Sacco,[†] Diana Hidalgo,[†,‡] Edvige Celasco,[†] and Candido Fabrizio Pirri[†,‡]

[†]Center for Space Human Robotics @PoliTo, Istituto Italiano di Tecnologia, C.so Trento 21, 10129 Torino, Italy
[‡]Department of Applied Science and Technology, Politecnico di Torino, C.so Duca degli Abruzzi 24, 10129 Torino, Italy
[§]ENSERG, Minatec, Grenoble Institute of Technology, parvis Louis Néel, 3, 38016, Grenoble, France

S *Supporting Information*

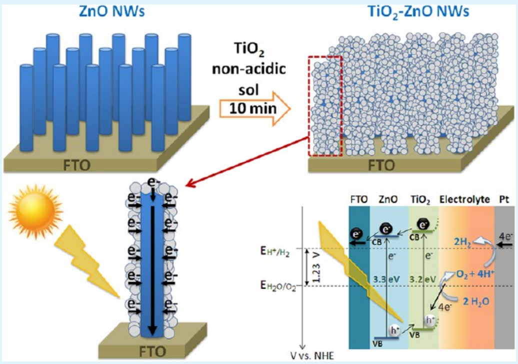

ABSTRACT: A fast and low-cost sol–gel synthesis used to deposit a shell of TiO$_2$ anatase onto an array of vertically aligned ZnO nanowires (NWs) is reported in this paper. The influence of the annealing atmosphere (air or N$_2$) and of the NWs preannealing process, before TiO$_2$ deposition, on both the physicochemical characteristics and photoelectrochemical (PEC) performance of the resulting heterostructure, was studied. The efficient application of the ZnO@TiO$_2$ core–shells for the PEC water-splitting reaction, under simulated solar light illumination (AM 1.5G) solar light illumination in basic media, is here reported for the first time. This application has had a dual function: to enhance the photoactivity of pristine ZnO NWs and to increase the photodegradation stability, because of the protective role of the TiO$_2$ shell. It was found that an air treatment induces a better charge separation and a lower carrier recombination, which in turn are responsible for an improvement in the PEC performance with respect to N$_2$-treated core–shell materials. Finally, a photocurrent of 0.40 mA/cm^2 at 1.23 V versus RHE (2.2 times with respect to the pristine ZnO NWs) was obtained. This achievement can be regarded as a valuable result, considering similar nanostructured electrodes reported in the literature for this application.

KEYWORDS: *ZnO nanowires, core–shell, TiO$_2$ nanoparticles, water splitting, photocatalysis, one-dimensional nanostructure*

1. INTRODUCTION

The development of technologies for a better exploitation of renewable energy sources is one of the major challenges in our society.[1] Among the renewable power sources, photocatalytic water splitting, also known as "artificial photosynthesis," offers a promising way for the clean, low-cost, and environmentally friendly production of hydrogen by solar energy.[2] In this context, the development of photoelectrochemical (PEC) cells for H$_2$ production with high stability over time (~25 years) and efficiency of at least 15% is mandatory to induce a breakthrough in the daily usage of this technology.[3]

Metal oxide semiconductors have been widely studied as photoanodes for PEC cells because they satisfy several criteria, such as appropriate band gap and flat band potential, low cost, low electrical resistance, and good scalability for production purposes. Among these semiconductors, titanium dioxide (TiO$_2$) is one of the most promising oxide materials to be used as a photoanode for water oxidation. TiO$_2$ offers the advantages of being abundant and stable in aqueous solutions under irradiation, as well as having a strong photocatalytic activity under UV light irradiation.[4,5] Zinc oxide (ZnO) is another abundant semiconductor that has similar properties, band gap and band edge positions to TiO$_2$, and it is one of the wide-band gap semiconductors that exhibits high electron mobility (1000 cm^2 V s^{-1} for single nanowires).[6−8] However, ZnO also suffers from the drawback of being low photocorrosion resistant in most electrolytic media.[9] The stability issue of ZnO in long-term applications therefore needs to be addressed.

The coupling of ZnO and TiO$_2$ in heterojunctions has been well-documented in literature reports,[10−13] where ZnO@TiO$_2$ materials have demonstrated a superior PEC activity, due to improved electron–hole separation and a lower recombination of charge carriers. Such features are in fact highly desirable to enhance the efficiency of PEC devices, such as dye-sensitized solar cells (DSSCs)[6] and PEC water-splitting cells.[14,15] Several methods, such as chemical vapor deposition,[16] atomic layer deposition,[17,18] and radio frequency magnetron sputtering,[19,20]

Received: March 7, 2014
Accepted: July 1, 2014
Published: July 1, 2014

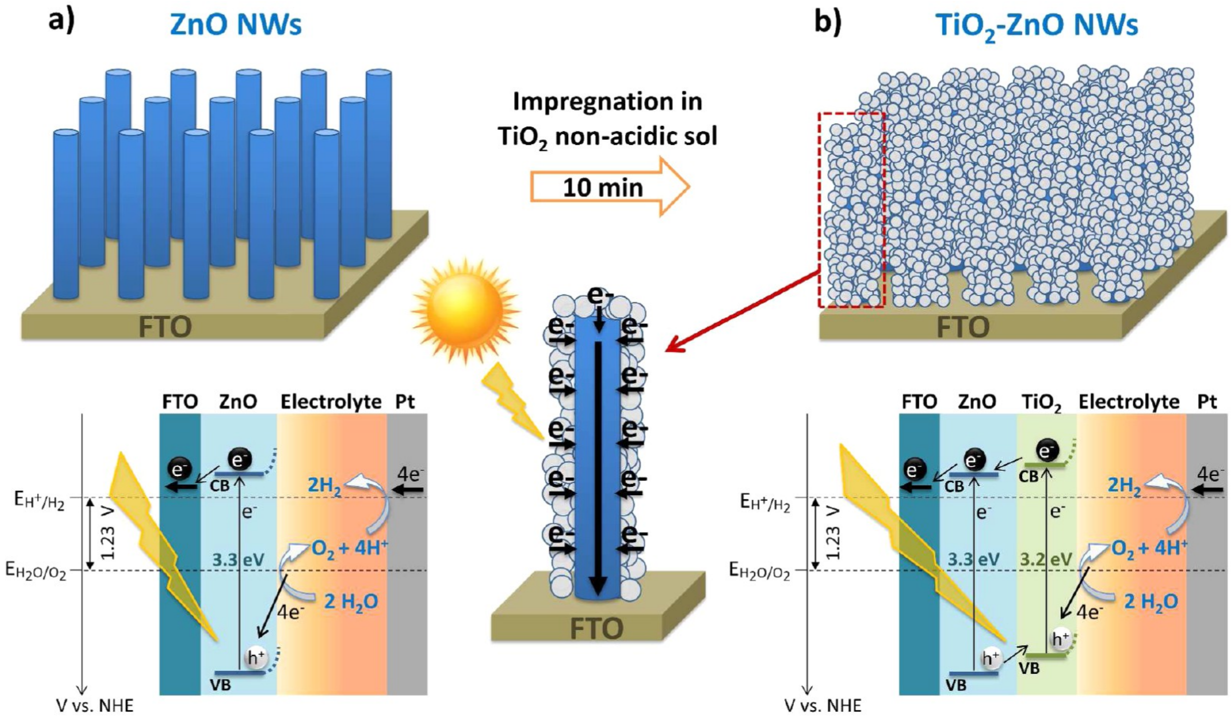

Figure 1. Scheme of the prepared photoelectrodes, consisting of (a) ZnO NWs and (b) ZnO@TiO_2 core−shell heterostructures and their band diagrams, which represent the charge carrier transport at the different water-splitting PEC cell interfaces.

have been explored to fabricate ZnO@TiO_2 core−shell heterostructures for use as photoanodes in solar cells. However, despite their high degree of control over the shell thickness, these techniques are expensive and not versatile to produce the large-area coverage of substrates. In addition, the low growth rates and modest material yields also constitute disadvantages. Some low-cost wet-chemical methods have recently been reported. For example, a layer-by-layer deposition procedure has been used to obtain a rutile TiO_2 shell on the surface of ZnO NWs, but it required up to 40 cycles to obtain a titania thickness of about 16 nm.[21] In another study, ZnO aggregates have been decorated with TiO_2 nanoparticles by immersing them into different titanium alkoxides precursors.[22] ZnO@TiO_2 core−shell heterostructures have also frequently been tested for the photocatalytic degradation of organic substances.[12,23,24] However, to the best of authors' knowledge, only one paper has reported the effect of a TiO_2 coating layer on the performance and stability of one-dimensional (1D) ZnO photoanodes for PEC water splitting.[25] In this work, Fan et al. dealt with Cl-doped ZnO NWs covered by TiO_2 shells of tunable thickness obtained through up to 100 successive adsorption−hydrolysis−condensation steps. This growth procedure, being a quasi atomic-layer one, results in a process that requires at least 60 repeated preparation steps to obtain about a 45 nm-thick TiO_2 shell; in addition, the maximum measured photocurrent density, under global air mass coefficient 1.5 (AM 1.5G) illumination, is lower than 1 μA/cm^2 for an applied potential of 1 V versus Ag/AgCl.

In the present paper, a simple, low-cost and rapid sol−gel synthesis procedure is reported for the deposition of a protective shell of anatase TiO_2 nanoparticles onto an array of vertically oriented ZnO NWs. In this procedure only 10 min are necessary to deposit a compact shell of crystalline anatase. Most importantly, an efficient application of such a core−shell ZnO@TiO_2 heterostructure for the PEC water-splitting reaction, which leads to photocurrent values that are 3 orders of magnitude higher than those reported in the literature for similar materials, is shown for the first time.[25]

In addition, the effect of postannealing on the synthesized ZnO@TiO_2 core−shells has been studied under two different gas atmospheres, namely air and nitrogen. Annealing of the photoelectrode material is one of the post-treatments that could have a significant effect on the PEC properties,[26] and several methods have been proposed.[27] In general, the thermal treatment of oxide materials improves their crystallinity by reducing certain defect centers. In addition, it increases the connectivity among grains by reducing grain boundaries and charge recombination. The overall effect is an enhancement of the metal oxide crystalline quality, and thus an enhancement of the photoactivity. However, the atmospheres in which the synthesis and the postannealing are performed can also influence the PEC activity of the material. For example, the postannealing of both ZnO (1D and two-dimensional (2D)) nanostructures and TiO_2 nanotubes in a nitrogen atmosphere has been found to further improve the PEC performance compared to non-annealed materials.[26,28] Thus, the influence of the annealing atmosphere (using both air and nitrogen) on the physicochemical characteristics (e.g., morphology, crystallinity, chemical composition, optical and electronic properties) of the resulting nanostructures has been investigated in depth in this work. The effect of a preannealing of the pristine ZnO NWs, before TiO_2 covering, on the PEC activity has also been studied, to match the optimized preparation conditions to the best PEC performance.

A representative scheme of the two kinds of ZnO photoelectrodes studied in this work is reported in Figure 1, together with their relative simplified band diagrams. An electron−hole pair is formed in the ZnO NWs (Figure 1a), upon absorption of an impinging photon. If the collection efficiency rate is adequate (i.e., the charge recombination probability is low enough), a considerable number of conduction band (CB) electrons is collected at the F-doped tin oxide (FTO) substrate before recombination. Meanwhile, the high-energy holes in the valence band (VB) move toward the interface with the electrolyte, where they oxidize the water. Consequently, a photocurrent is observed at negative potentials with respect to the water oxidation (WO) redox potential (E^oO_2/H_2O = 1.23 V vs reversible hydrogen electrode (RHE)), since some of the energy required for WO is provided by the radiation. The presence of the TiO_2 shell in the core−shell nanostructure (Figure 1b) improves the charge separation efficiency, thanks to the presence of a potential barrier at the semiconductor/electrolyte interface, which limits the charge recombination. Therefore, in ZnO@TiO_2 core−shell nanostructures, the high electron mobility within the 1D ZnO nanocrystals, which is exploited for a fast transport toward the FTO, is coupled with the efficient separation of charge carriers between the TiO_2 shell and the ZnO core.

Finally, a comparative study that points out the reasons for the improved performance of the ZnO@TiO_2 core−shell photoanode under sunlight illumination, with respect to both pristine ZnO NWs and a film of equivalent thickness of TiO_2 nanoparticles,[29,30] was also conducted.

2. EXPERIMENTAL SECTION

2.1. Synthesis of the Core−Shell ZnO@TiO_2 Heterostructures. A vertical array of ZnO nanowires was grown following a two-step synthetic approach, as previously reported,[31,32] on an FTO conductive layer deposited on glass (7 Ω/sq from Solaronix) with 4 × 2 cm^2 dimensions. The first synthetic step consists of the deposition of a thin (about 10 nm) and oriented polycrystalline ZnO film, called seed layer. To prepare the seed layer, an ethanol solution of 10 mM zinc acetate (99.99%, Sigma) was deposited, by spin coating, on a 2 × 2 cm^2 area of the FTO substrate and then thermally treated at 350 °C for 20 min (heating rate 5 °C/min) in air. The obtained ZnO polycrystalline seed-layer was able to further direct the growth of the nanowires, which occurred under a hydrothermal route. The seeded substrates were immersed for 2 h at 88 °C under stirring into an aqueous solution containing zinc nitrate hexahydrate (purity 98%, Sigma) and hexamethylenetetramine (HMT, purity 99.5%, Sigma) with a Zn^{2+}/HMT molar ratio of 2:1, 5 mM polyethylenimine (M_W = 800, end-capped, Sigma) and 320 mM ammonium hydroxide. The final volume was adjusted to 50 mL. The samples were then removed from the solution, washed thoroughly with bidistilled water, and dried in a gentle stream of nitrogen.

The titania shell was deposited on the ZnO nanowires using a non-acid sol−gel synthesis solution.[33] First, a solution of 0.46 M titanium isopropoxide (TTIP, 97%, Sigma) and 0.28 M acetylacetone (99%, Fisher Aldrich) was prepared in 5 mL of 1-butanol (anhydrous, 99.8%, Sigma) as a solvent, under vigorous stirring. The FTO-glass substrates with the ZnO nanowires were placed vertically into this solution, facing the beaker center, under stirring (300 rpm) at room temperature. The reaction started as soon as 0.92 M bidistilled water was injected into the synthesis solution; the substrates were then removed after 10 min and dried in air.

A first set of core−shell samples was annealed either in air (sample ZT-air-A) or in nitrogen (sample ZT-N_2-A), both at 450 °C for 30 min (heating rate = 1 °C/min), to promote the crystallization of the titania shell in the anatase phase and remove the organic moieties.

Reference samples were also prepared by annealing the ZnO NWs either in air (the Z-air-A sample) or in nitrogen (Z-N_2-A) at 450 °C for 30 min. Another experimental condition was considered for comparison purposes, which involved annealing the ZnO nanowires in air at 450 °C for 30 min (heating rate = 1 °C/min), prior to the titania deposition. After the TiO_2 deposition, the obtained core−shell sample (named ZT-air-B) was treated in air at 450 °C for 30 min, as in the case of the previous samples. All the thermal steps used to prepare the different samples are reported in the Supporting Information (Table S1) for ease of comparison.

The reference sample containing a film of TiO_2 nanoparticles (NPs) was prepared using a previously reported sol−gel procedure,[29,30] to compare the PEC activity of this material, which was also annealed in air at 450 °C for 30 min, with those of the bare ZnO NWs and of ZnO@TiO_2 core−shell samples.

2.2. Morphological and Structural Characterization. The pristine ZnO and core−shell ZnO@TiO_2 morphology was characterized by means of a ZEISS Auriga field emission scanning electron microscope (FESEM) in top and cross section views, while the elemental analysis (energy dispersive spectroscopy, EDS) was carried out by means of an Oxford Inca XSight detector.

The crystalline structure was analyzed using a PANalytical X'Pert X-ray diffractometer in the Bragg−Brentano configuration. Cu Kα monochromatic radiation was used as the X-ray source, with a characteristic wavelength of λ = 1.540 59 Å.

Transmission electron microscopy (TEM) was performed with a FEI Tecnai F20ST operating at 200 kV, to evaluate the quality and crystallinity of the ZnO core and the TiO_2 shell in the bright-field TEM (BF-TEM), high-resolution TEM (HRTEM), scanning TEM (STEM), and electron diffraction (ED) modes. EDS was performed with an EDAX detector. The samples for the TEM characterization were scratched from the substrate and dispersed in HPLC ultrapure ethanol for 2 min by means of sonication. Then, a dispersion drop was placed onto a holey carbon−copper grid and left to dry.

UV−visible spectra were recorded in transmittance and total reflectance modes (specular and diffuse), with a Cary 5000 Scan UV−visible spectrophotometer, using a total reflectance sphere. All the spectra were background subtracted.

X-ray photoelectron spectroscopy (XPS) characterizations were carried out with a Versa Probe5000 (Physical Electronics) equipped with a monochromatic X-ray source Al Kα (1486.6 eV). A beam diameter of a 100 μm size was employed to investigate the chemical composition of the surface. All analyses were obtained with a combined electron and low-energy ion argon beam neutralization system. The binding energy of the XPS was calibrated on the Ag 3d 5/2 lines at Eb = 368.25 eV, according to literature.[34]

2.3. Photoelectrochemical Characterization. The PEC experiments were performed in a Teflon reactor equipped with a quartz window for frontal illumination (see Figure S1 of the Supporting Information). All the tests were carried out in a three-electrode configuration using the ZnO, ZnO@TiO_2, or TiO_2 materials as the working electrodes for the water-photoelectrolysis reaction, a platinum wire as the counter electrode, and Ag/AgCl (KCl 3 M) as the reference electrode, in 0.1 M NaOH aqueous electrolyte (pH = 12.7). The measurements were recorded using a multichannel VSP potentiostat/galvanostat produced by BioLogic, with EC-Lab software, version 10.1x, for data acquisition. Current−voltage (I−V) characteristic curves and photoactivity tests were recorded by means of linear sweep voltammetry (LSV) at a scan rate of 10 $mV\cdot s^{-1}$, when a constant open circuit voltage was achieved, varying the applied potential from −0.7 to 0.7 V versus Ag/AgCl, in the dark and under AM 1.5G sunlight illumination (450 W Xe lamp by Newport with an AM 1.5 filter and a water filter model 6123NS), with a power density of 100 mW/cm^2. The irradiance was measured by means of a Delta Ohm Photoradiometer model HD2102.1. Chrono-amperometric (I−t) tests were carried out to examine the photoresponse of the ZnO, ZnO@TiO_2, and TiO_2 structures over time, at −0.1 and +0.2 V versus Ag/AgCl under continuous on−off light cycles with the same illumination condition used for the LSV.

The measured potentials versus the Ag/AgCl reference electrode were converted to the RHE scale via the Nernst eq 1:

$$E_{\mathrm{RHE}} = E_{\mathrm{Ag/AgCl}} + 0.059\mathrm{pH} + E^{\circ}_{\mathrm{Ag/AgCl}} \quad (1)$$

where E_{RHE} is the converted potential versus RHE, $E_{\mathrm{Ag/AgCl}}$ is the experimental potential measured against the Ag/AgCl reference electrode, and $E^o{}_{\mathrm{Ag/AgCl}}$ is the standard potential of Ag/AgCl (KCl 3 M) at 25 °C (i.e., 0.210 V).

Incident photon-to-electron conversion efficiency (IPCE) spectra were recorded using a Newport Xe lamp (150 W) coupled to a monochromator (Cornerstone 130 by Newport), by varying the wavelength of the incident light from 300 to 550 nm (step size: 10 nm), at an applied potential of −0.1 V versus Ag/AgCl. In this case, the electrode illuminated area was 1 cm^2, and the light power density was about 1 mW/cm^{-2} (measured at 390 nm).

Electrochemical impedance spectroscopy (EIS) curves were recorded using the same potentiostat described above, in the dark and under simulated solar light, from 0.1 Hz to 1 MHz, with an alternating current (AC) amplitude of 25 mV, at an applied potential of −0.1 V versus Ag/AgCl. The EIS measurements for the Mott−Schottky plots were performed at frequencies of 10, 7.5, and 5 kHz with an AC amplitude of 20 mV, varying the potential from −0.8 to 0.7 V versus Ag/AgCl, with a scan step of 0.1 V.

3. RESULTS AND DISCUSSION

3.1. Study of the Different Annealing Atmospheres (Air Versus N_2).

3.1.1. Morphology and Structure. Vertically oriented ZnO NWs, about 1.5−2 μm long and 100−150 nm wide, were obtained by means of hydrothermal synthesis on the FTO substrates. Top view FESEM images of the samples that were thermally treated in air (Z-air-A) and N_2 (Z-N_2-A) are reported in Figure 2a,c, respectively. No significant morphological differences can be observed between these samples. The FESEM images of the core−shell ZnO@TiO_2 structures annealed in the air (ZT-air-A) and N_2 (ZT-N_2-A) atmospheres are reported in Figure 2b,d, respectively. In both cases, it can be observed that after 10 min of impregnation of the ZnO NWs in the titania sol, a quite uniform covering of the NWs was obtained, with a slight increase in the titania shell thickness close to the top of the NWs. In addition, the STEM and TEM images reported in Figure 3 highlight the TiO_2 shell with a variable thickness (between 20 and 50 nm) uniformly covering the ZnO NWs surface, after both the air and N_2 atmosphere treatments. The STEM image and the relative EDS maps in Figure 3a correspond to the ZT-air-A sample. A detail of the interface between the monocrystalline ZnO core and the polycrystalline TiO_2 shell, of the same sample, is shown in the HRTEM image and the fast Fourier transform (FFT) insets in Figure 3b. The TEM and HRTEM images in Figure 3c,d,e, also show the presence of a polycrystalline and randomly oriented layer of TiO_2 (see the FFT in the insets of Figure 3d) on a monocrystalline (002)-oriented ZnO structure for the ZT-N_2-A sample. As a first consideration, there is no evidence, from the FESEM and TEM analyses, of any substantial morphological difference between the two different core−shell samples. The TiO_2 layer seems to adhere very well to the ZnO surface and to create a continuous shell structure. This result was attributed to the high control on the nucleation of the titania on the ZnO surface. In fact, it has been reported that the hydrolysis and condensation rates of titanium isopropoxide (i.e., the titania precursor used in this work) in butyl alcohol solutions are faster than the same reactions when other titanium alkoxides (e.g., tetrabutyl titanate) are used.[22] However, such reactions take place in a more controlled way if acetylacetone is added as the chelating agent.[33] Hence, since the TTIP is dissolved in a butyl alcohol/acetylacetone solution, the hydrolysis and condensation steps can only occur after the gradual addition of water. This leads to the direct polymerization of the Ti−O−Ti networks on the surface of the ZnO material, which results in the controlled nucleation of small titania nanoparticles. As a consequence, the final thickness of the crystalline TiO_2 shell, which is observed after the annealing step, depends on the impregnation time of the ZnO NWs in the TiO_2 sol (such a correlation is discussed in the aforementioned published paper[29]).

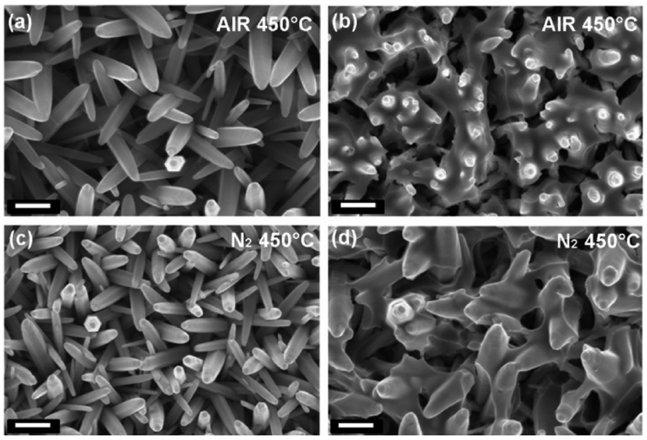

Figure 2. FESEM images (top view) of the ZnO NWs and core−shell ZnO@TiO_2 nanostructures. Samples annealed in air at 450 °C: (a) Z-air-A, (b) ZT-air-A. Samples thermally treated in N_2 at 450 °C: (c) Z-N_2-A, (d) ZT-N_2-A. The scale bars are all set to 500 nm.

The X-ray diffraction (XRD) patterns of pristine ZnO NWs (Z-air-A sample, dashed red line in Figure 4a, and the Z-N_2-A sample, dashed blue line in Figure 4b) show the peaks related to the wurtzitic crystalline phase of ZnO and highlight a preferential orientation of ZnO NWs along the (002) crystalline axis. Some differences between the two annealing atmospheres of the core−shell samples were found. In the case of the thermal treatment in air (ZT-air-A sample, straight red line in Figure 4a), the completely hidden signal of TiO_2 was attributed to the small size of the formed crystals.[35] This result is in agreement with the TEM images, in which the FFT had pointed out the presence of TiO_2 crystals (Figure 3b). The existence of TiO_2 in the ZT-air-A sample has also been confirmed by the EDS analysis (reported in Figure 3a and in the Supporting Information, Figure S2), which shows the presence of both Zn and Ti elements. As far as the thermal treatment in the N_2 atmosphere (ZT-N_2-A sample, straight blue line in Figure 4b) is concerned, a small peak at 25.3°, corresponding to the (101) plane of the anatase phase of crystalline TiO_2, is clearly visible. Such a result is in agreement with the HRTEM characterization of the sample shown in Figure 3e, which indicates some TiO_2 crystals ranging from 4 to 10 nm. An amorphous contribution was also observed in the XRD pattern in the 15°−35° range, where an increase in the background signal was observed, which was more pronounced than the sample annealed in air.

On the basis of this analysis, it can be argued that the different annealing conditions influence the crystallization and growth processes of the TiO_2 nanoparticles and, as a consequence, the interconnection and carrier transport among the titania particles. All these features can affect the final performance of the core−shell structure in the PEC cell, as will be discussed hereafter.

3.1.2. XPS Surface Analysis. An XPS analysis was performed on the pristine ZnO NWs samples and on the ZnO@TiO_2 core−shell nanostructures, to confirm the presence of the TiO_2 shell and to understand whether some nitrogen doping was present on the N_2-treated samples. The survey spectra (Figure S3, Supporting Information) confirmed the successful titania

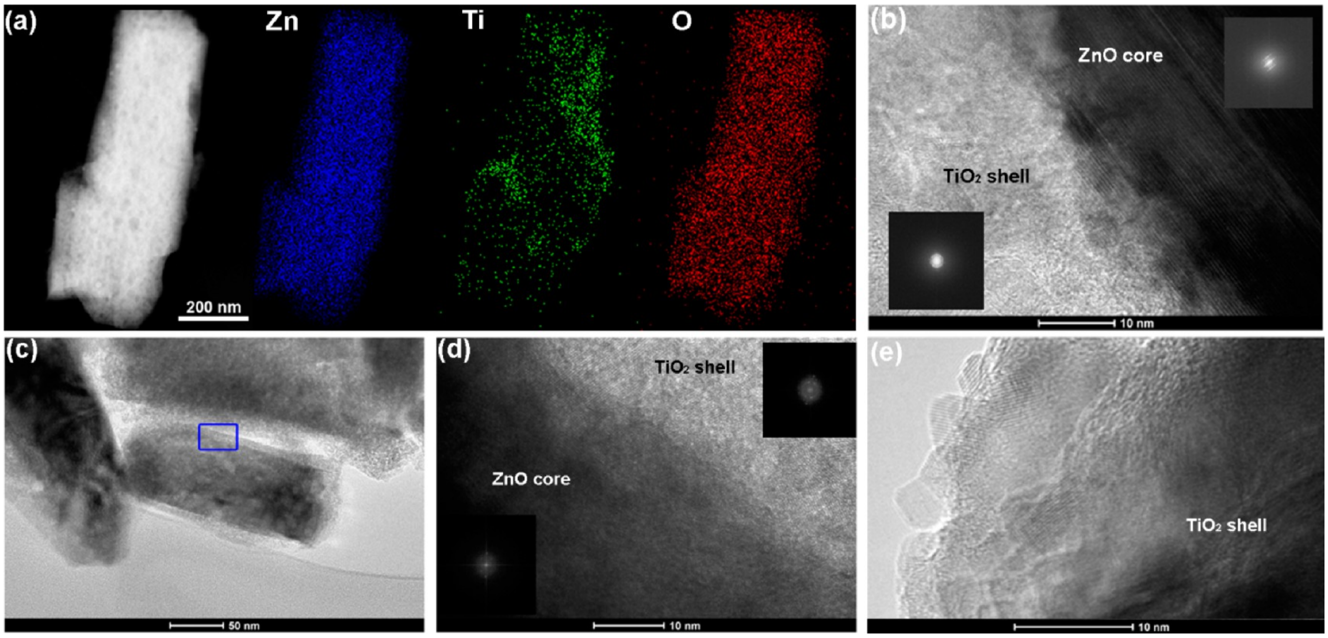

Figure 3. STEM with EDS maps (a) and TEM images (b−d) of the core−shell ZnO@TiO$_2$ heterostructures annealed in both air, ZT-air-A (a, b), and in N$_2$, ZT-N$_2$-A (c, d). The FFT of the ZnO cores and the TiO$_2$ shells are shown in the insets of (b, d), respectively. (e) HRTEM on the TiO$_2$ shell of the ZT-N$_2$-A sample.

deposition on the ZnO NWs. Regarding the role of the N$_2$ treatment, the N 1s peak related to the surface nitrogen atoms was detected in the survey spectra of both the Z-N$_2$-A and the ZT-N$_2$-A samples (Supporting Information, Figure S3c,d) at a binding energy of around 400 eV. The presence of such a peak was also confirmed in the high-resolution spectra of the same samples (Figure 4c), which showed a broad peak between 395.5 and 402.5 eV in both cases. The N 1s peak of oxinitride (O−Zn−N) in N-doped ZnO[15] is usually found between the typical binding energies of zinc nitride (396−397 eV).[36] However, the N 1s peak of the Z-N$_2$-A sample was centered at around 399 eV. On the other hand, in the case of N-doped TiO$_2$, a peak should be present at ∼396 eV,[37] but this was not observed in the examined core−shell samples. A N 1s peak centered at ∼400 eV, is usually present in nitrogen-treated TiO$_2$ samples and is attributed to either interstitial N atoms or chemisorbed N$_2$ molecules at the TiO$_2$ surface.[37,38] Therefore, it is possible to conclude that, in the present samples, the N atoms were most probably chemisorbed on the surface of either the ZnO NWs or TiO$_2$ shell, or introduced into the crystalline structure, thus creating some interstitial defects in both the Z-N$_2$-A and ZT-N$_2$-A samples.

A detailed deconvolution study on the high-resolution O 1s peaks was also performed for all the studied samples, treated either in air or in nitrogen atmospheres (see Figure S4 and Table S2 in the Supporting Information). The samples treated in nitrogen (Z-N$_2$-A and ZT-N$_2$-A) evidenced an increment in the highest energy binding shoulder of the O 1s peak (at about 532 eV), which in the literature has been associated with hydroxyl groups that are strongly bound to surface defects in both ZnO[39] and TiO$_2$.[40] This evidence confirms the previous hypothesis of a high concentration of oxygen vacancies or defects in the nitrogen-treated samples.

3.1.3. Optical Properties. UV−vis spectroscopy, both in transmittance and total reflectance modes (specular and diffuse), was performed to point out the influence on the optical properties of the TiO$_2$ deposition on the ZnO NWs. The absorbance, obtained as $A = 1 - R - T$ (where A is the absorbance, T is the transmittance, and R is the total reflectance), is reported in Figure 5a as a function of the wavelength in the region between 350 and 800 nm. The effect of the TiO$_2$ layer, for both the air and N$_2$ treatment conditions, is to increase the light absorption, compared to the pristine ZnO NWs, especially in the visible region.

The successful covering of the ZnO NWs and the role of the TiO$_2$ shell were also confirmed by the total reflectance and the Kubelka−Munk spectra reported in Figure 5b,c, respectively, as a function of wavelength in the UV range. An enhanced reflectance of the core−shell samples with respect to the pristine ZnO NWs is evident in these plots, which show lower values of the Kubelka−Munk function, $F(R)$, this function being $F(R) = (1 - R)^2/2R = k/s$, where k is the molar absorption coefficient and s is the scattering coefficient. These results can be attributed to different contributions. First, differences in the morphology and size of the two semiconductor nanostructures might have played a role. In fact, ZnO NWs have a high surface-to-volume ratio, and thus an enhanced scattering in the UV region should be expected for the core−shell samples. The core−shell structures, in fact, show an increase in both the surface roughness and surface area, due to the titania nanoparticles that constitute the shell.[41] In addition, the TiO$_2$ film covering the ZnO NWs can induce constructive interference effects between the rays reflected from the different interfaces, thus increasing the total reflectance. Finally, in the UV region, $F(R)$ is generally higher for nanostructured films made of ZnO than for similar films made of TiO$_2$.

The optical band gap (E_g) of the samples was calculated using the Tauc's method[42] from the $F(R)$ spectra. According to this method, the plot of $[F(R)h\nu]^n$ against $h\nu$ shows a linear region just above the optical absorption edge, where $n = 2$ is used for the direct allowed transition, $n = 1/2$ for the indirect allowed transition, and $h\nu$ is the photon energy (eV). Both the experimental results and theoretical calculations suggest that

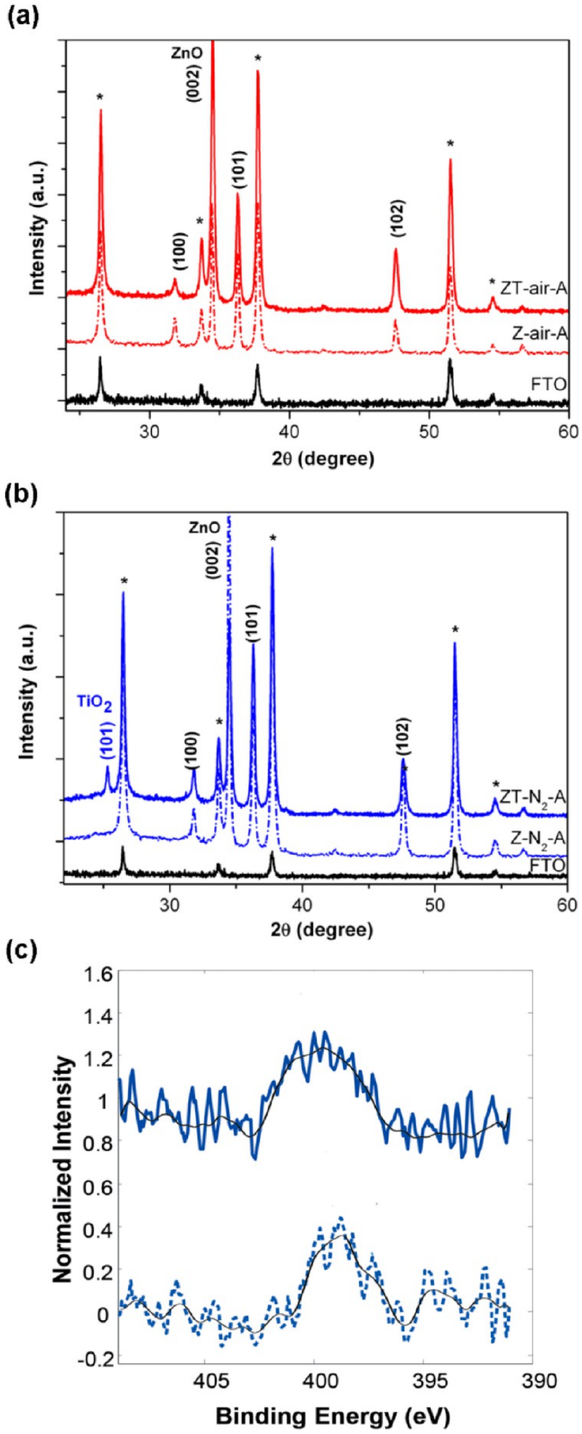

Figure 4. X-ray diffraction patterns of the ZnO NWs and ZnO@TiO$_2$ core–shell nanostructures: (a) samples annealed in air, and (b) samples annealed in nitrogen. The spectrum of the FTO substrate is also reported for an easy comparison (black curve); the asterisks (*) refer to the related diffraction peaks. (c) The XPS high-resolution spectra of the N 1s signal of the Z-N$_2$-A (dotted blue line) and ZT-N$_2$-A (straight blue line) samples. The straight black lines in (c) represent the average smoothing of the curves.

the ZnO and TiO$_2$ nanoparticles have a direct forbidden gap.[24,42−44] Hence, in the Tauc plot shown in Figure 5d, $n = 2$ was employed, which clearly yields a satisfactory linearity for both the ZnO NWs and ZnO@TiO$_2$ core–shell samples. The resulting E_g values are reported in Table 1. In this context, a small but expected reduction in the band gap in both core–shell samples can be observed with respect to the pristine ZnO NWs.

The reduction in the band gap and the increased visible light absorption on the core–shell ZnO@TiO$_2$ materials can be attributed to different factors. The first factor is due to the combined effect of the E_g of ZnO (~3.3 eV) and the relatively lower E_g of anatase TiO$_2$ (~3.2 eV), which results in the narrowing of the overall band gap on the ZnO@TiO$_2$ heterostructure.[24] In addition, the increase in the surface area, which was attributed to the deposition of the TiO$_2$ nanoparticles on the ZnO NWs surface, leads to surface states within the gap that effectively reduce the band gap, as previously reported.[41,45]

As far as the N$_2$-treated samples are concerned, both the Z-N$_2$-A and ZT-N$_2$-A materials show a higher absorption of the UV and visible light than the air-annealed samples (see Figure 5a). Such a result corresponds to the slightly lower values of the band gap observed for these samples in Table 1, thus indicating the formation of an allowed energy level within the band gap.[28,38] In agreement with the XPS analysis, these impurity levels could be attributed to the creation of oxygen vacancies during the thermal treatment, which produce intrinsic defects in both the ZnO NWs and TiO$_2$ nanoparticles in the shell. This in turn can affect the PEC performance of the material in two opposite ways. First, electron–hole pairs produced at the photoelectrode–electrolyte interface under light illumination can recombine in the defect centers, thereby reducing the generated current.[46] On the other hand, these defects, which act as light harvesters in the longest wavelength region (as observed in the absorbance spectra in Figure 5a), could work as active centers for the water-splitting reaction.[26] However, in the present work (see Figure 1), only the high-energy photons corresponding to wavelengths lower than 400 nm are able to activate the photocatalytic reaction. Thus, the first effect prevails over the second one, as it is the reason for the worse PEC behavior of the nitrogen-treated materials than the ones annealed in air, which will be shown in the following sections.

3.1.4. Photoelectrochemical Properties. To gain information about the carrier density and the flat-band potential at the semiconductor–electrolyte interface, EIS measurements have been performed on the different ZnO NWs and ZnO@TiO$_2$ core–shell nanostructures.[14] The flat-band potential is one of the most important parameters for semiconductor electrodes because it determines the band edge positions at the semiconductor–electrolyte interface and thus fixes the energies of the conduction band electrons and valence band holes that react with the electrolyte solution.[47] The flat-band potential was determined, for all the samples, from the extrapolation of the x-axis intercepts in the Mott–Schottky plots ($1/C^2$ versus V) at various frequencies. The plots at 7.5 kHz are reported in the Supporting Information (Figure S5) as a representative example, since the measurements performed at other frequencies lead to similar results. The curves are in agreement with the expected behavior of an n-type semiconductor: a linear increase in the capacitance (C) can be observed as the applied bias potentials (V) increase, until a plateau value is reached.[48] Moreover, the differences between all the samples can be appreciated. As shown in Table 1, the flat-band potential is shifted toward more negative values for both core–shell structures, and the samples subjected to annealing in air are characterized by the lowest flat-band potentials. On the basis of these results, a preliminary conclusion can be made: to have an

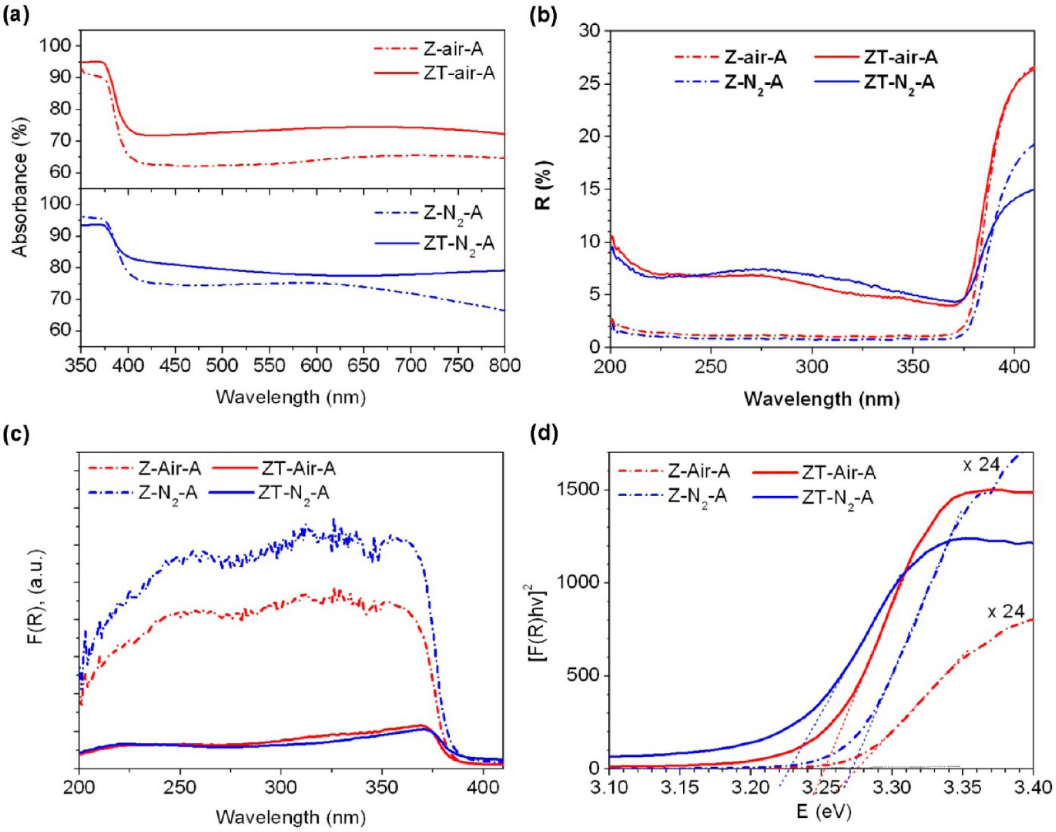

Figure 5. UV−vis spectra of the pristine ZnO NWs (dashed-dotted curves) and the ZnO@TiO_2 core−shell nanostructures (straight curves) treated in either air or N_2 atmospheres: (a) absorbance, (b) total reflectance, (c) Kubelka−Munk function, and (d) Tauc plot for the band gap calculation.

Table 1. Properties of Pristine the ZnO and Core-Shell ZnO@TiO_2 Samples

sample	band gap (E_g, eV)	flat band (E_{FB}, V vs RHE)	donor density[a] (N_d, cm^{-3})	maximum STH efficiency[b] (η_{MAX}, %)	potential at η_{MAX}[b] ($E\eta_{MAX}$, V vs RHE)
Z-air-A	3.28	−0.03	$1.26e^{18}$	0.027	0.94
ZT-air-A	3.25	−0.66	$3.75e^{17}$	0.039	0.88
Z-N_2-A	3.27	0.23	$1.80e^{18}$	0.019	0.99
ZT-N_2-A	3.22	−0.08	$6.98e^{17}$	0.031	0.89

[a]These donor density values were calculated from the EIS measurements at the 7.5 kHz frequency. [b]Data obtained from Figures 6c,d.

efficient photocatalyst, characterized by as much negative flat-band potential as possible, the best solution is to coat the ZnO NWs with TiO_2 and perform the annealing process in air.

To evaluate the donor density of the different nanostructures, the Mott−Schottky plots were fitted in the linear region and eq 2 was exploited.[47]

$$\frac{1}{{C_{SC}}^2} = \frac{2}{e\cdot\varepsilon\cdot\varepsilon_0\cdot N_d}\left(E - E_{FB} - \frac{kT}{e}\right) \tag{2}$$

where C_{SC} is the capacitance of the space charge region, ε_0 is the permittivity of the free space, ε is the dielectric constant of the semiconductor (10 for ZnO, 19 for the core−shell samples, calculated as a weighted volume value between the ε of both ZnO and TiO_2), N_d is the donor density, e is the electron charge value, E is the applied potential, E_{FB} is the flat-band potential, and kT/e is the temperature-dependent correction term (25 mV at room temperature).

The values obtained from the linear fitting process (reported in Table 1) are comparable with those usually observed for ZnO NWs (in the 10^{17}−10^{18} cm^{-3} range).[49] The donor density of the ZnO NWs (Z-air-A) and core−shell sample (ZT-air-A) treated in air are lower than the respective nitrogen annealed samples (Z-N_2-A and ZT-N_2-A). This result had been expected because of the previous discussion on the band gap of the N_2 treated samples, and it confirms that a thermal treatment in an O_2-poor atmosphere could lead to an increase in oxygen vacancies in the nanowire structure, which act as donor species.[50] On the other hand, the core−shell samples exhibit lower donor density values than the pristine ZnO samples. From the discussion above, it follows that the use of core−shell nanostructures could pave the way to the fabrication of highly efficient PEC devices for the water-splitting reaction. In fact, the lower donor density of the core−shell samples could lead to higher charge carrier mobility, thus allowing a larger flowing current than the bare ZnO NWs samples.[52]

3.1.5. Photoelectrochemical Activity for the Water-Splitting Reaction. The PEC activity of the ZnO NWs and the ZnO@TiO_2 heterostructures was evaluated in a 0.1 M NaOH solution (pH = 12.7), using the prepared electrodes as photoanodes for the water-photoelectrolysis reaction. This electrolyte was chosen to evaluate also the stability of the core−shell materials in comparison with the pristine ZnO NWs, since

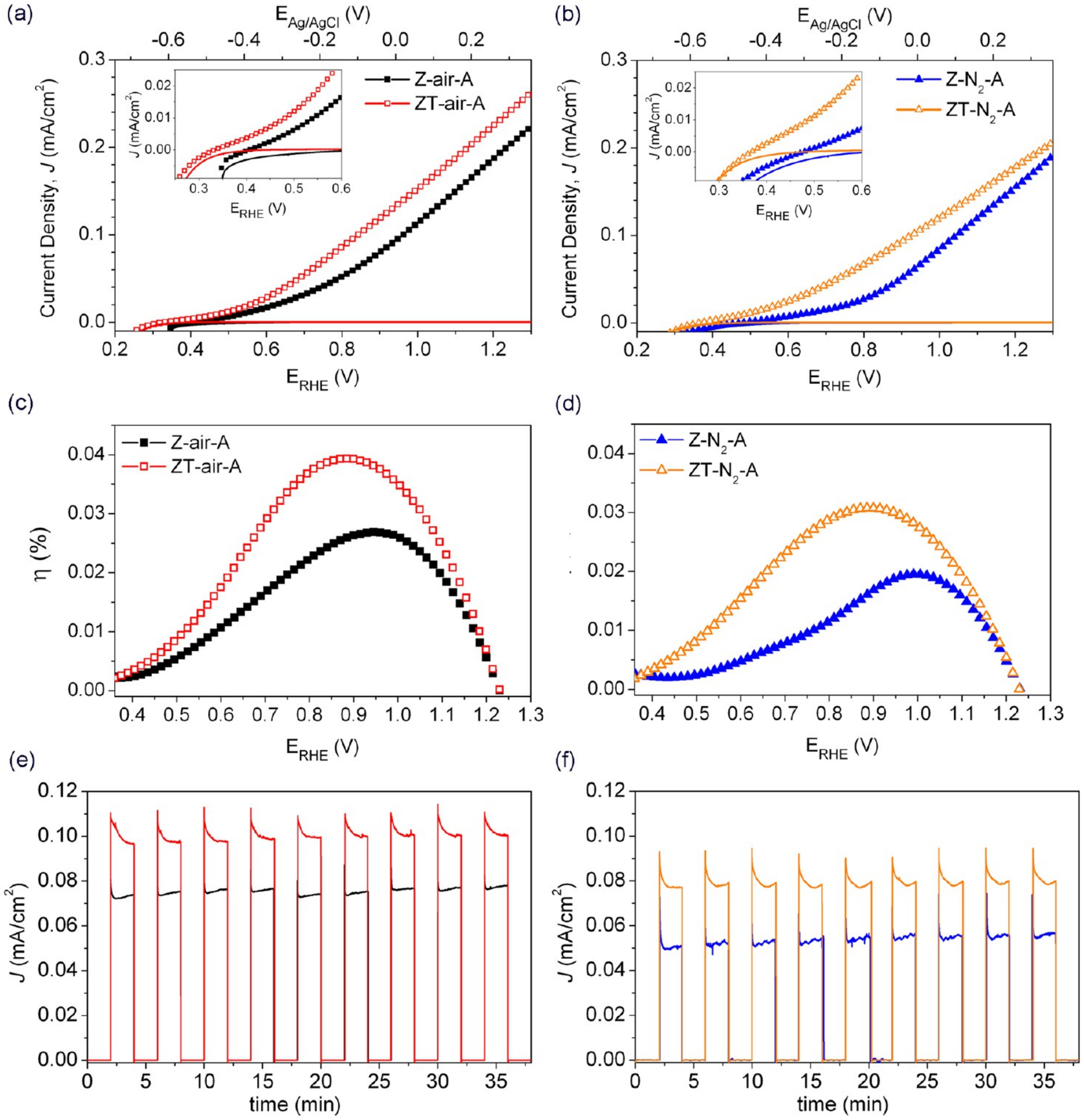

Figure 6. (a, b) *I*−*V* curves measured in the dark (continuous line) and under simulated solar light (AM 1.5G, 100 mW/cm^2) (discrete points), (c, d) solar-to-hydrogen efficiency, and (e, f) chrono-amperometry measurements, over continuous on-off light cycles at 0.85 V vs RHE, of the pristine ZnO NWs and ZnO@TiO$_2$ heterostructures annealed in both air and N$_2$ atmospheres.

the latter are less chemically stable in basic or acidic solutions under light illumination.[9]

Figure 6a,b reports the *I*−*V* curves of the pristine ZnO NWs and the ZnO@TiO$_2$ heterostructures annealed in air and in N$_2$, respectively, in the dark and under simulated AM 1.5G solar light. Even though the UV light only contributes 4% to the total sunlight spectra, the core−shell samples showed higher photocurrent values and a negative shift of the onset potential for the water-splitting reaction under illumination than the pristine ZnO NWs annealed in the same conditions. As far as the first point is concerned, the increased photocurrents should be attributed to two main causes: (1) enhanced light absorption in the UV region, in accordance with the results of the optical measurements; (2) improved electron−hole separation efficiency (which represents one of the main outcomes of the usage of core−shell nanostructures), which was investigated through EIS measurements (see below). As far as the shift of the onset potential is concerned, this finding can be explained by considering the previous discussion on the flat-band potentials of the ZnO@TiO$_2$ core−shell heterostructures (see Table 1 and Section 3.1.4). In fact, both the ZnO NWs and the ZnO@TiO$_2$ core−shells behave as n-type semiconductors, and a depletion layer exists for positive potentials of the flat band; that is, the band edges curve upward at the semiconductor−electrolyte interface as shown in Figure 1. Thus, upon irradiation in such a space-charged region, the photogenerated electrons exploit the high e^- mobility within the 1D ZnO nanostructure while moving toward the FTO substrate (Figure 1a). The high-energy holes remaining in the valence band (VB) move toward the interface with the electrolyte and oxidize the water. In particular there is a synergic photogeneration and separation of the charge carriers between the TiO$_2$ shell and in the ZnO core, in the ZnO@TiO$_2$ (see Figure 1b). Similarly, a more negative E_{FB} value causes a larger driving force for the electrons, thus implying a shift in the conduction band (CB) edge toward higher energies and an increase in the total current flowing into the material. Hence, the lower flat-band potential of the ZnO@TiO_2 core−shells, coupled with the higher absorption of the UV light, results in higher photocurrents being obtained at lower potentials.

The solar-to-hydrogen (STH) efficiency (η) of each sample under sunlight was calculated from the $I-V$ data according to eq 3:[50]

$$\eta = J(1.23 - E_{\mathrm{RHE}})/I_{\mathrm{light}} \qquad (3)$$

where E_{RHE} is the applied bias versus RHE, J is the photocurrent density at the measured bias voltage, and I_{light} is the irradiance intensity (equal to 100 mW/cm^{-2} for AM 1.5G).

As expected, the η curves follow the previously found trend, that is, the materials treated in air show higher efficiency values (Figure 6c) than those annealed in the N_2 atmosphere (Figure 6d). The maximum of the STH efficiency curves (η_{MAX}, reported in Table 1) increases in the following order: Z-N_2-A < ZT-N_2-A < Z-air-A < ZT-air-A. In addition, a left-shift on the STH efficiency peak to lower potential values for both the core−shell heterostructures is evident (see Table 1 and Figure 6c,d). These results are in good agreement with the left-shift observed in the flat-band potential and the onset of the water-oxidation reaction of the ZnO@TiO_2 core−shells, with respect to the pristine ZnO NWs (annealed under the same conditions), and imply that a lower potential is required for the core−shell samples than for ZnO NWs to obtain the maximum efficiency.

In addition, Figure 6e,f shows the $I-t$ curves of all the ZnO and ZnO@TiO_2 samples biased at −0.1 V versus Ag/AgCl (0.85 V vs RHE), that is a potential around which the η_{MAX} was obtained for all the materials. In general, a good photocurrent stability was observed for all the samples under numerous on-off light cycles for a period of 40 min. Stability was also examined at a higher potential (1.2 V vs RHE) for a longer time (90 min), after which no losses in current density were observed (see Supporting Information, Figure S6). Here in particular, the ZT-air-A sample reached a photocurrent density of 0.19 mA/cm^2 (35% higher than the photocurrent observed for the ZT-N_2-A sample).

The observed photocurrent densities and η_{MAX} are in-line with and, in some cases, even better than the literature values obtained for both pure and doped ZnO NWs and 1D TiO_2−ZnO nanostructures, tested for the water-photoelectrolysis reaction under AM 1.5G simulated sunlight. For instance, Hsu and Chen[51] reported photocurrent densities below 50 μA/cm^2 at 1.23 V_{RHE} for ZnO and Al-doped ZnO (AZO) nanorod arrays about 1 μm-long, as well as η_{MAX} of 0.01% and 0.02% (at a bias of about 1.4 V_{RHE}) for ZnO and AZO nanorod arrays modified with a pretreatment in H_2; Yang et al.[15] reported photocurrent densities of about 0.025 and 0.25 mA/cm^2 at 1.23 V_{RHE} under neutral pH with ZnO NWs and N-doped ZnO NWs, respectively; Ji et al.[10] obtained less than 0.13 mA/cm^2 at 1.23 V_{RHE} using rutile TiO_2 nanorods both with and without a shell of ZnO nanoparticles. Apart from these considerations, it is worth noting that the present core−shell samples exhibit higher photocurrent densities than those reported in literature when a similar Cl-doped ZnO NWs covered with a TiO_2 shell[25] was used. In fact, Fan et al.[25] reported photocurrents lower than 1 μA/cm^2 at 1 $V_{\mathrm{Ag/AgCl}}$, which have been attributed to the compactness and low surface area of the TiO_2 shell. Therefore, one of the advantages of the synthesis procedure here employed regards the high surface area of the TiO_2 shell, which contributes positively by increasing the number of reactive sites at the photocatalyst surface, with a resulting improved performance of our ZnO@TiO_2 material.

IPCE measurements were performed to study the photoactive wavelength regime for the ZnO and ZnO@TiO_2 nanostructures. Figure 7a reports the spectra related to the samples treated in air. In general, the IPCE curves are able to reproduce the shape of the absorption and total reflectance spectra of both the ZnO and ZnO@TiO_2 materials in the UV region quite well (see Figure 5a−c for a comparison). The ZT-air-A sample shows lower IPCE values than the pristine ZnO NWs at lower wavelengths than 350 nm, probably because of the higher scattering of the UV light in this region, which limits the light absorption in the ZnO core. However, in agreement with the absorption spectra shown in Figure 5a, higher IPCE values can be observed for the core−shell in the 350−400 nm range, this being the reason for the higher total photocurrent exhibited by the core−shell nanostructures under the solar spectrum than the pristine ZnO NWs.

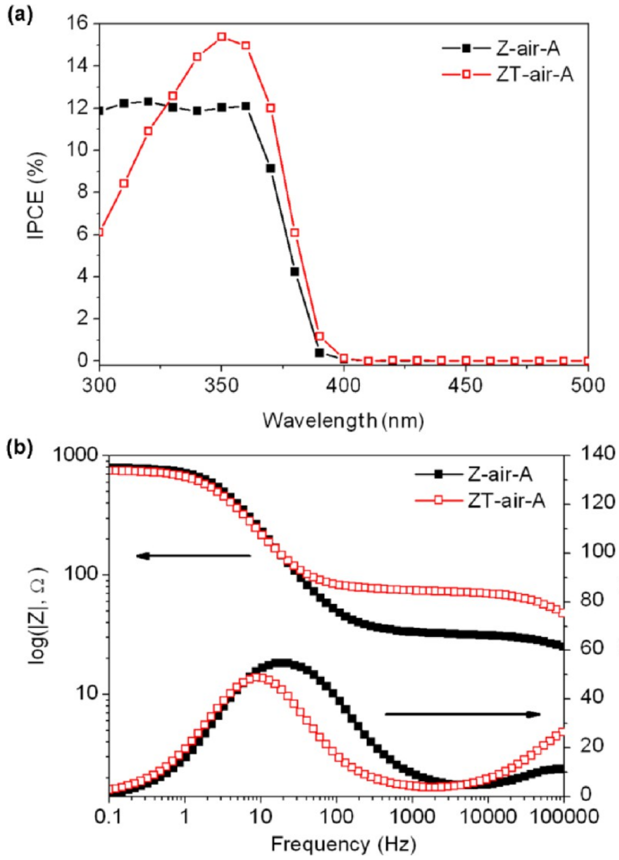

Figure 7. (a) IPCE spectra of the pristine ZnO NWs and ZnO@TiO_2 heterostructures annealed in air, at an applied potential of 0.85 V vs RHE. (b) Modulus and phase Bode plots of EIS measurements on the Z-air-A and ZT-air-A samples.

Lower IPCE values were measured for the samples annealed in N_2 than for the sample annealed in air (data not shown), in accordance with the $I-V$ characterization. The lower STH efficiencies and IPCE values related to the N_2-annealed samples can be attributed to the interstitial defects and oxygen vacancies of either the ZnO or the titania shell, in the ZnO NWs and ZnO@TiO_2 samples, respectively. In both cases, such impurity levels act as electron−hole recombination centers, and this effect is considered to be predominant, despite the slightly

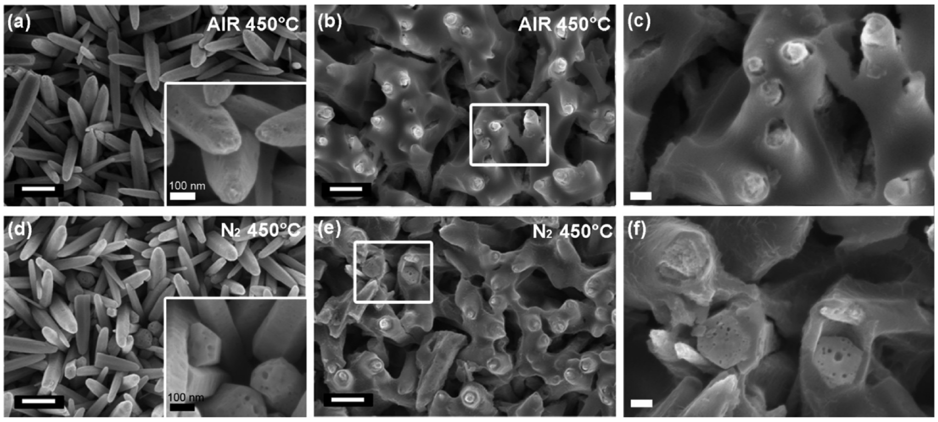

Figure 8. FESEM images (top views) of the bare ZnO NWs and core−shell ZnO@TiO_2 nanostructures after the PEC measurements: samples annealed in air (a) Z-air-A, (b, c) ZT-air-A, and in nitrogen (d) Z-N_2-A, (e, f) ZT-N_2-A. The scale bars are all set to 500 nm, except for (c, f) where the scale bars are set to 100 nm; (c, f) show a higher magnification of the white squares shown in (b, e).

higher visible light absorption (and lower band gap) of the N_2-treated samples. In addition, the contribution of the amorphous part in the N_2-annealed samples (as mentioned for the XRD analysis) probably reduces the carrier mobility in the ZnO NWs, thus leading to a consequent lower PEC performance of these photoelectrodes than the air-treated ones.

The increased PEC performance of the core−shell structures, compared to that of the pristine ZnO NWs, can be attributed not only to the high surface area of the TiO_2 shell, the lower flat-band potential and the improved UV−vis absorption of the core−shell sample (as discussed above), but also to the improved photoelectron collection mechanism, which includes photoelectron injection and charge transport. The photoelectron injection is mainly due to the charge-transfer across the photoanode−electrolyte interface. As previously mentioned, it can be supposed that the TiO_2 acts as a chemical passivation layer on the ZnO surface; in addition, the better interaction of TiO_2 with common electrolyte solutions is beneficial for photoelectron injection. Both effects can reduce the charge recombination rate in the core−shell samples compared to the pristine ZnO NWs annealed in the same conditions. To confirm this hypothesis, EIS measurements were performed on the different samples. The Bode plots of modulus and phase of the structures annealed in air are reported in Figure 7b as an example. As can clearly be observed, the low-frequency phase peak (in the 1−1000 Hz range, associated with the charge recombination)[52] of the core−shell ZT-air-A sample is shifted toward lower values than the pristine ZnO NWs, which means a longer charge lifetime. On the other hand, the frequency of the other peak (above 1 kHz, associated with the transport properties inside the material),[53] related to the TiO_2-covered ZnO, is higher than that of the pristine NWs. This implies a slightly lower charge transport time, with beneficial effects on the collection efficiency and, as a consequence, on the photocurrent density values.

Finally, to investigate the ability of the TiO_2 shell layer to protect the ZnO NWs core from photocorrosion, all the samples were systematically tested for about 5 h in the NaOH electrolyte solution, and after this operational period, the morphology and appearance of the materials were checked. The FESEM images and a photograph of the pristine ZnO NWs and of the core−shell samples after the PEC tests are reported in Figure 8 and in the Supporting Information, Figure S7. A remarkable degradation of the uncovered ZnO material can easily be observed at both the macro- and nanoscopic levels. In particular several holes were formed on the ZnO surface for both the ZnO NWs samples treated either in air or in the N_2 atmospheres, and some material was sufficiently corroded to detach from the FTO surface (see Supporting Information, Figure S7). Some damage is also evident in the core−shell structure treated in N_2 (ZT-N_2-A), in a region where the top of the ZnO NWs is covered less by the TiO_2 (Figure 8d). In addition, unlike the core−shell sample treated in air, it can be seen that a modification of the ZT-N_2-A structure has also extended to the titania layer, where some flakes appear on the surface (Figure 8e,f).

3.2. Influence of the ZnO NW Preannealing on the Core−Shell Properties and Performance.

3.2.1. Structural and Optical Properties. Owing to the degradation of the ZnO material during the PEC tests and to the positive effect of the thermal treatment in air, it was decided to perform a pretreatment by annealing the pristine ZnO NWs (at 450 °C for 30 min in air) before impregnation in the titania sol, thus synthesizing the ZT-air-B sample. It was expected that this preliminary thermal treatment on the ZnO would consolidate the crystalline structure, and also induce a change in the wetting properties of its surface and consequently in the resulting characteristics of the TiO_2 shell. It was previously reported[54] that pristine ZnO nanowires, after a hydrothermal synthesis, exhibited a pronounced hydrophilic behavior, due to the presence of hydroxyl groups bound to zinc atoms (≡Zn−OH) on the surface. The thermal treatment at 450 °C should have condensed the hydroxyl groups, led to oxylane groups (≡Zn−O−Zn≡), desorbed the resulting water molecules, and finally turned the surface properties from hydrophilic to hydrophobic. This would have favored the wetting behavior of the titania precursor solution in 1-butanol on the hydrophobic ZnO surface (see the Experimental Section).

The structural, morphological, and optical characterization of the ZT-air-B sample is reported in Figure 9. FESEM and BF-TEM images (Figure 9a,b), as well as the EDS maps in Figure 9c (of the region highlighted in Figure 9b), clearly show a uniform coverage of the TiO_2 shell on the ZnO NWs. In addition, it is worth noting the presence of the (101) reflection of the anatase phase in the X-ray diffraction pattern (Figure 9d), together with the peaks related to the wurtzite phase of the ZnO. As a consequence, by comparing the XRD pattern of this sample with that of ZT-air-A sample, it can be noted that the

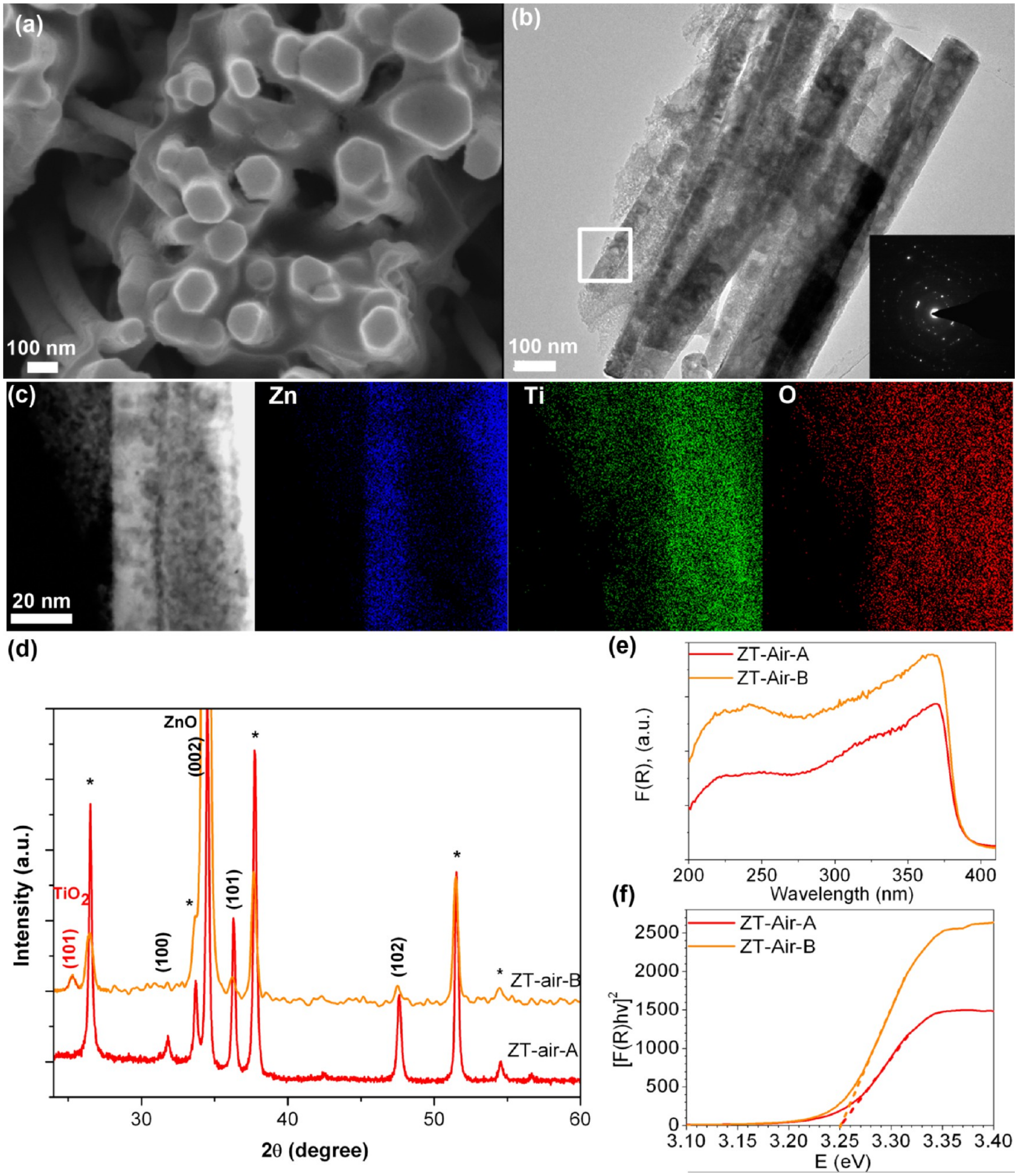

Figure 9. (a) FESEM and (b) BF-TEM images of the ZnO@TiO$_2$ core−shell sample ZT-Air-B. The diffraction pattern is shown in the inset of (b). (c) EDS maps of the region highlighted in (b). (d) XRD, (e) UV−vis spectrum and (f) Tauc plot for the band gap calculation of the ZT-air-B sample compared with the ZT-air-A sample.

pretreatment had a positive effect on promoting the crystallization of TiO$_2$. The presence of a polycrystalline, randomly oriented layer of TiO$_2$ on a monocrystalline ZnO structure was also confirmed for this sample (see FFT in the insets of Figure 9b). Moreover, as shown in Figure 9e,f, the absorbance of the UV light of the ZT-air-B sample increased compared to the ZT-air-A sample, while they exhibited a similar band gap, thus demonstrating an even less defective structure in the ZT-air-B sample, due to the higher crystallinity obtained in both the ZnO core and the TiO$_2$ shell. It is possible to speculate that the increased crystallinity and the large size of the titania crystallites are due to the hydrophobic behavior of the

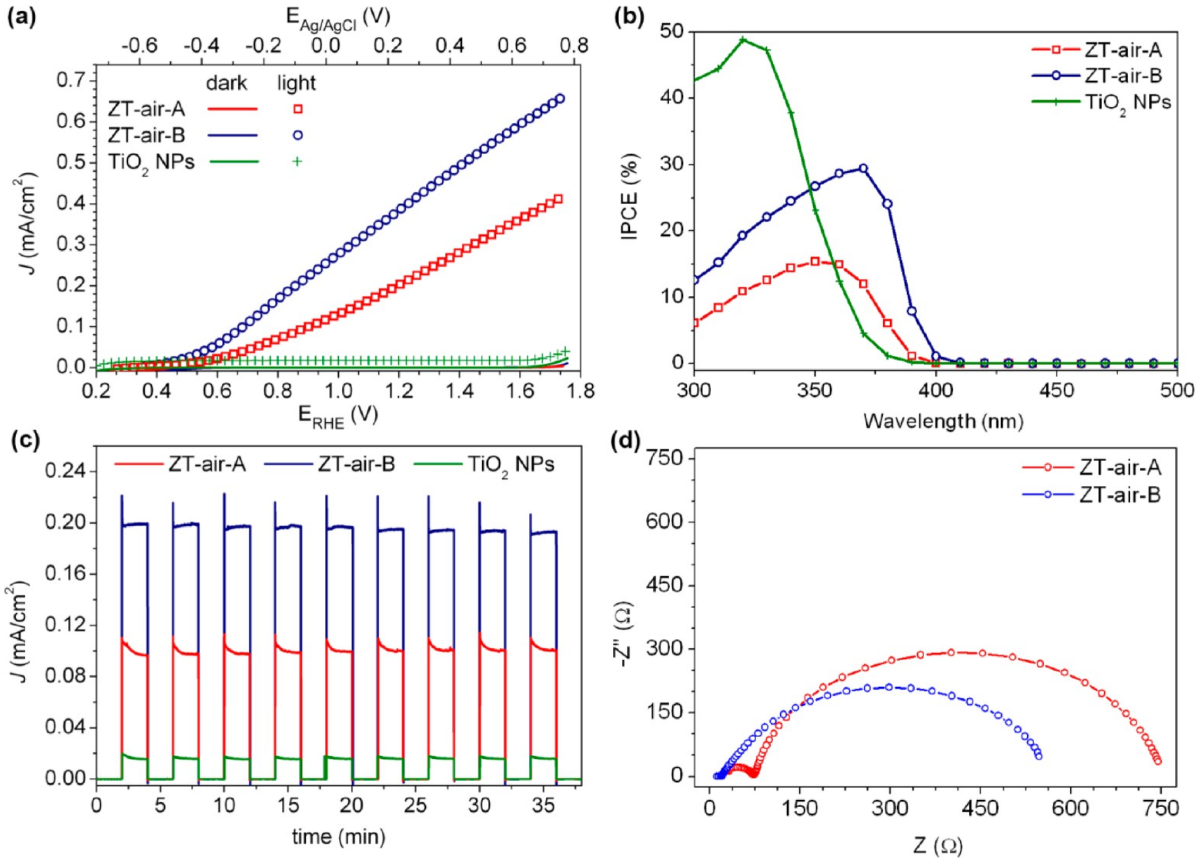

Figure 10. Photoelectrochemical tests of the ZnO@TiO_2 core−shell photoanodes made without (ZT-air-A) and with (ZT-air-B) preannealing of the ZnO NWs before the TiO_2 impregnation, in comparison with a TiO_2 NPs film of equivalent thickness. (a) *I*−*V* curves in the dark and under simulated sunlight (AM 1.5G, 100 mW/cm^2). (b) IPCE, (c) chrono-amperometry curves over on-off light cycles, and (d) Nyquist plots at an applied potential of −0.1 V vs Ag/AgCl (0.85 V vs RHE).

ZnO surface, obtained after the pretreatment at 450 °C, which improved the nucleation and growth of the anatase crystals during the impregnation step.

3.2.2. Photoelectrochemical Performance and Comparison with a TiO_2 Film.

The results of the PEC tests performed on the core−shell ZT-air-B sample are reported in Figure 10, where they are compared with the results obtained for the core−shell ZT-air-A sample, prepared without ZnO preannealing. As expected, the improved crystalline quality of the preannealed ZnO NWs in the core−shell ZT-air-B structure has led to higher photocurrent values than those of the ZT-air-A sample. For instance, the ZT-air-B sample produces a photocurrent of 0.40 mA/cm^2 at 1.23 V versus RHE, about twice the photocurrent obtained from the ZT-air-A sample, which generates 0.21 mA/cm^2 at the same potential.

In addition, PEC measurements were performed on a TiO_2 film, with an equivalent thickness to the height of the ZnO NWs (about 2 μm), which was constituted by policrystalline anatase nanoparticles (NPs) of about 9 nm in size.[29] It is worth noting the superior activity of both of the ZnO@TiO_2 core−shell samples (ZT-air-A and ZT-air-B), which show 15 and 24 times higher photocurrents, respectively, at 1.23 V versus RHE than the TiO_2 NPs film. Moreover, the η_{MAX} of the ZT-air-B sample is 0.075% (at 0.85 V vs RHE), this being 2.2 times higher than that of the ZT-air-A sample, while the TiO_2 NPs film exhibits a η_{MAX} of 0.015% (at 0.28 V vs RHE), and thus is 5 times lower than the best one of the core−shell materials. These results are confirmed by the IPCE spectra presented in Figure 10b, where the curve of the ZT-air-B photoanode surpasses those of both the ZT-air-A and TiO_2 NPs samples at wavelengths higher than 360 nm. In fact, even though the TiO_2 NPs sample evidenced a maximum IPCE of about 50% at 320 nm, the lower quantum yield (below 10%) at higher wavelengths than 360 nm (at which the AM 1.5G solar spectrum starts to contribute) is the main reason for the reduced performance of this TiO_2 film under sunlight illumination.

Finally, the chrono-amperometric curves at 0.85 and 1.2 V versus RHE of both the core−shell samples and of the TiO_2 film (reported in Figure 10c and in the Supporting Information, Figure S6) show an optimal repeatability and stability of the photocurrent along numerous on-off light cycles. Moreover, in accordance with the previous results, the ZT-air-B sample reports up to 2.2 and 24 times higher current densities than the ones measured for the electrodes with the ZT-air-A core−shell and with the TiO_2 NPs, respectively.

In addition, the morphology of the core−shell structure of the ZT-air-B sample after the electrochemical tests (reported in Figure S8 in the Supporting Information) shows almost no alteration or damage to either the ZnO or the TiO_2 materials (see Figure 9a for a comparison with the same sample before the operation in PEC), thus confirming its stability for prolonged use as water-oxidation photocatalyst.

These PEC results confirm that the thermal pretreatment of the ZnO nanostructures is effective in enhancing the crystalline quality of the material, and therefore the pretreatment probably improves the electron transport inside the 1D nanostructure. In addition, the high hydrophobicity of the ZnO NWs after the preannealing likely favors the interconnection between the ZnO NWs and the TiO_2 crystallites, thus further improving the electronic transport and separation of the carriers at the ZnO−TiO_2 interface and reducing the carrier recombination. The improvement in both these properties was assessed through impedance spectroscopy analysis. The Nyquist plots of the ZT-air-A and ZT-air-B samples are reported in Figure 10d. As is clearly evident, both arcs related to the charge transport (i.e., on the left), and to the charge recombination (i.e., on the right) in the Nyquist plot are smaller for the preannealed sample, thus implying a faster electronic transport inside the nanostructures as well as a more efficient charge separation.

It is worth noting that the reported activity of the core−shell ZT-air-B sample is in-line with recent results on pure and N-doped rutile TiO_2 NWs (~1.6 μm).[37] In addition, in some cases it has overcome the performance of low band gap semiconductor thin films prepared by means of wet chemical techniques,[55] such as Fe_2O_3, WO_3/Fe_2O_3, $SrTiO_3$, $BiVO_4$,[56] and $WO_3/BiVO_4$.[57] In most of the latter cases, the reduced performance is due to the planar morphology, low surface area, and high charge carrier recombination that prevails toward the high visible light absorption of the material, which causes low IPCE values (below 10%).

Nonetheless, the photocurrents obtained with the core−shell sample are still lower than those recently obtained through a combination of 1D nanostructuration, doping, cocatalysis, and sensitization with low band gap semiconductors (i.e., CdS and CdSe). For instance, a photocurrent of 1.6 mA/cm^2 has been obtained for a $WO_3/BiVO_4$ nanorod by Su et. al,[57] due to the high surface area and better charge transport within the 1D nanostructure, which has a maximum IPCE of 12% and an action spectra until 500 nm. Still higher values (about 2.4 mA/cm^2 at 1.23 V_{RHE}) have been obtained with Mo-doped $BiVO_4$, thanks to the 4-fold increase in the IPCE (almost constant at 40% for $\lambda < 460$ nm) compared to nondoped $BiVO_4$ films, due to the reduced charge-transfer resistance.[56] Cobalt has been also used by Hoang et al.[37] to cocatalyze N-doped TiO_2 NWs, and an increase has been obtained in both the IPCE (up to 20% from 420 to 470 nm) and the photocurrent (0.8 mA/cm^2 at 1.7 V_{RHE}). Cobalt treatment has been found to play a dual role: first, the passivation of surface states, thus increasing holes lifetime, and second, the formation of a Co-based water-oxidation catalyst layer. Moreover, the low band gaps of CdSe and CdS (about 2.4 eV) have been suggested to be responsible for an increase in the visible light absorption and IPCE spectrum to 650 nm. Ji et al.[10] have deposited CdSe in both TiO_2 NWs and TiO_2 NWs@ZnO heterojunctions, and up to 0.7 and 1.7 mA/cm^2 were obtained, respectively. Hsu et. al[51] used CdS as a sensitizer in H_2-treated AZO nanorods, and their photocurrent was increased to about 4 mA/cm^2 and 4% of η_{MAX}.

This analysis suggests that further improvement in the PEC performance of the ZnO@TiO_2 core−shell materials could be obtained by exploiting one or more of the previous listed approaches, such as by synthesizing hybrid structures with low band gap semiconductors or by codoping/cocatalyzing, to achieve the standards expected for commercial implications.

4. CONCLUSIONS

A fast sol−gel synthesis procedure adopted to obtain ZnO@TiO_2 core−shell nanostructures for application as photoanodes for the PEC water-splitting reaction has been reported in this work. After the growth of ZnO nanowires by means of the hydrothermal route on FTO substrates, the titania shell was deposited, upon impregnation in a sol, after which high coverage levels of the ZnO NWs surface were obtained after only 10 min of immersion. The presence of acetylacetone in the titania precursor solution induces a slowing down of the hydrolysis rate and thus led to a controlled deposition of the titania shell.

The role of the gas atmosphere during the annealing step has been studied in depth. An anatase crystalline structure of the TiO_2 layer on wurtzite ZnO NWs was obtained after a thermal treatment either in air or in a nitrogen atmosphere. Both the air and N_2-treated core−shell ZnO@TiO_2 nanostructures produced enhancements of the photocurrent of about 28% and 40% as well as of the maximum STH efficiency of 44% and 63%, respectively, in comparison to the pristine ZnO NWs treated in the same atmosphere. However, it was noted that the thermal treatment in air was more beneficial to the PEC performances than the annealing in nitrogen.

A further enhancement of the photocurrent was obtained with 2.2 times higher values for the air-annealed core−shell sample by preannealing the ZnO NWs before the TiO_2 deposition (ZT-air-B sample). Such a process leads to the consolidation of the ZnO crystals, their greater wettability being experienced by the titania precursor solution, and a better interconnection at the ZnO−TiO_2 interphase. Moreover, this latter core−shell exhibited 24 times higher photocurrents at 1.23 V versus RHE than a TiO_2 NPs film of equivalent thickness. Finally, a lower degradation of the ZnO NWs in the core−shell structures was observed thanks to the presence of the TiO_2 protective shell. This degradation was further reduced by the prethermal treatment of ZnO NWs prior to the titania deposition. The thus-optimized synthesis procedure and thermal treatments lead to a core−shell material that has enhanced photocatalytic properties for the water-oxidation reaction compared to bare ZnO NWs, TiO_2 NPs film, to similar Cl-doped ZnONWs@TiO_2, and to other planar thin films of visible light-absorbing materials[55] (e.g., Fe_2O_3, WO_3/Fe_2O_3, $SrTiO_3$, $BiVO_4$,[56] and $WO_3/BiVO_4$[57]).

It can therefore be concluded that the anatase titania shell on ZnO NWs plays a double role. First, it protects the ZnO NWs structure, and long-term lifetimes of the core−shell photoanodes for the water-splitting reaction are thus obtained. Second, the TiO_2 shell treated in air increases the PEC performances, favors charge separation and reduces the charge recombination. The thermal treatment in the nitrogen atmosphere instead produces a higher number of defects in both crystalline structures, which reduces the PEC performances in comparison with the air-annealed photoanodes.

In conclusion, the efficient application of the ZnO@TiO_2 core−shell photoanodes opens important perspectives, not only in the water-splitting application field, but more in general for other photocatalytic applications (e.g., photovoltaic cells and degradation of organic substances), due to their chemical stability and easiness of preparation. Their high specific surface area and improved light-scattering ability can also be exploited for coupling to either low band-gap semiconductors (i.e., CdSe or CdS, among others) or cocatalysts, to further increase their IPCE and action spectrum in the visible wavelengths, and consequently achieve the efficiency required for commercial applications.

ASSOCIATED CONTENT

Supporting Information

Detailed synthesis of the core−shell ZnO@TiO_2 nanostructures, a description of the cell used for the PEC measurements, the EDS and XPS (survey and O 1s high resolution spectra) characterization results, the Mott−Schottky plots, long-time current behavior of the ZnO@TiO_2 core−shell samples (i−t curves), pictures of pristine ZnO NWs and core−shell samples and FESEM image of the ZT-air-B sample after PEC tests. This material is available free of charge via the Internet at http://pubs.acs.org.

AUTHOR INFORMATION

Corresponding Author

*E-mail: simelys.hernandez@iit.it. Phone: +39.0110903418. Fax: +39.0110903401.

Notes

The authors declare no competing financial interest.

ACKNOWLEDGMENTS

The authors would like to thank Profs. E. Tresso and G. Saracco from the Politecnico di Torino for the fruitful discussions and advice. The financial support from the European Commission on the 7th Framework Program NMP-2012 Project ECO^2CO_2 nr.309701 is gratefully acknowledged.

REFERENCES

(1) Centi, G.; Perathoner, S. *The Chemical Element: Chemistry's Contribution to Our Global Future;* García-Martínez, J., Serrano-Torregrosa, E., Eds.; Wiley-VCH: Germany, 2011.

(2) Ni, M.; Leung, M. K. H.; Leung, D. Y. C.; Sumathy, K. A Review and Recent Developments in Photocatalytic Water-Splitting Using for Hydrogen Production. *Renewable Sustainable Energy Rev.* **2007**, *11*, 401−425.

(3) Newman, J.; Hoertz, P. G.; Bonino, C. A.; Trainham, J. A. Review: An Economic Perspective on Liquid Solar Fuels. *J. Electrochem. Soc.* **2012**, *159*, A1722−A1729.

(4) Fujishima, A.; Honda, K. Electrochemical Photolysis of Water at a Semiconductor Electrode. *Nature* **1972**, *238*, 37−38.

(5) Linsebigler, A. L.; Lu, G.; Yates, J. T. Photocatalysis on TiO_2 Surfaces: Principles, Mechanisms, and Selected Results. *Chem. Rev.* **1995**, *95*, 735−758.

(6) Anta, J. A.; Guillén, E.; Tena-Zaera, R. ZnO-Based Dye-Sensitized Solar Cells. *J. Phys. Chem. C* **2012**, *116*, 11413−11425.

(7) Zhang, Q.; Dandeneau, C. S.; Zhou, X.; Cao, G. ZnO Nanostructures for Dye-Sensitized Solar Cells. *Adv. Mater.* **2009**, *21*, 4087−4108.

(8) Gonzalez-Valls, I.; Lira-Cantu, M. Vertically-Aligned Nanostructures of ZnO for Excitonic Solar Cells: A Review. *Energy Environ. Sci.* **2009**, *2*, 19−34.

(9) Chou, T. P.; Zhang, Q.; Cao, G. Effects of Dye Loading Conditions on the Energy Conversion Efficiency of ZnO and TiO_2 Dye-Sensitized Solar Cells. *J. Phys. Chem. C* **2007**, *111*, 18804−18811.

(10) Ji, I. A.; Park, M.-J.; Jung, J.-Y.; Choi, M. J.; Lee, Y.-W.; Lee, J.-H.; Bang, J. H. One-Dimensional Core/Shell Structured TiO_2/ZnO Heterojunction for Improved Photoelectrochemical Performance. *Bull. Korean Chem. Soc.* **2012**, *33*, 2201.

(11) Lei, Y.; Zhao, G.; Liu, M.; Zhang, Z.; Tong, X.; Cao, T. Fabrication, Characterization, and Photoelectrocatalytic Application of ZnO Nanorods Grafted on Vertically Aligned TiO_2 Nanotubes. *J. Phys. Chem. C* **2009**, *113*, 19067−19076.

(12) Chen, D.; Zhang, H.; Hu, S.; Li, J. Preparation and Enhanced Photoelectrochemical Performance of Coupled Bicomponent ZnO−TiO_2 Nanocomposites. *J. Phys. Chem. C* **2007**, *112*, 117−122.

(13) Shaogui, Y.; Xie, Q.; Xinyong, L.; Yazi, L.; Shuo, C.; Guohua, C. Preparation, Characterization and Photoelectrocatalytic Properties of Nanocrystalline Fe_2O_3/TiO_2, ZnO/TiO_2, and Fe_2O_3/ZnO/TiO_2 Composite Film Electrodes towards Pentachlorophenol Degradation. *Phys. Chem. Chem. Phys.* **2004**, *6*, 659−664.

(14) Wolcott, A.; Smith, W. A.; Kuykendall, T. R.; Zhao, Y.; Zhang, J. Z. Photoelectrochemical Study of Nanostructured ZnO Thin Films for Hydrogen Generation from Water Splitting. *Adv. Funct. Mater.* **2009**, *19*, 1849−1856.

(15) Yang, X.; Wolcott, A.; Wang, G.; Sobo, A.; Fitzmorris, R. C.; Qian, F.; Zhang, J. Z.; Li, Y. Nitrogen-Doped ZnO Nanowire Arrays for Photoelectrochemical Water Splitting. *Nano Lett.* **2009**, *9*, 2331−2336.

(16) Irannejad, A.; Janghorban, K.; Tan, O. K.; Huang, H.; Lim, C. K.; Tan, P. Y.; Fang, X.; Chua, C. S.; Maleksaeedi, S.; Hejazi, S. M. H.; Shahjamali, M. M.; Ghaffari, M. Effect of the TiO_2 Shell Thickness on the Dye-Sensitized Ssolar Clls with ZnO−TiO_2 Core−Shell Nanorod Electrodes. *Electrochim. Acta* **2011**, *58*, 19−24.

(17) Greene, L. E.; Law, M.; Yuhas, B. D.; Yang, P. ZnO−TiO_2 Core−Shell Nanorod/P3HT Solar Cells. *J. Phys. Chem. C* **2007**, *111*, 18451−18456.

(18) Law, M.; Greene, L. E.; Radenovic, A.; Kuykendall, T.; Liphardt, J.; Yang, P. ZnO−Al_2O_3 and ZnO−TiO_2 Core−Shell Nanowire Dye-Sensitized Solar Cells. *J. Phys. Chem. B* **2006**, *110*, 22652−22663.

(19) Wang, M.; Huang, C.; Cao, Y.; Yu, Q.; Guo, W.; Huang, Q.; Liu, Y.; Huang, Z.; Huang, J.; Wang, H.; Deng, Z. The Effects of Shell Characteristics on the Current-Voltage Behaviors of Dye-Sensitized Solar Cells Based on ZnO/TiO_2 Core/Shell Arrays. *Appl. Phys. Lett.* **2009**, *94*, 263506−263506−3.

(20) Wang, M.; Huang, C.; Cao, Y.; Yu, Q.; Deng, Z.; Liu, Y.; Huang, Z.; Huang, J.; Huang, Q.; Guo, W.; Liang, J. Dye-Sensitized Solar Cells based on Nanoparticle-Decorated ZnO/TiO_2 Core/Shell Nanorod Aarrays. *J. Phys. D: Appl. Phys.* **2009**, *42*, 155104.

(21) Yin, X.; Que, W.; Fei, D.; Xie, H.; He, Z. Effect of TiO_2 Shell Layer Prepared by Wet-Chemical Method on the Photovoltaic Performance of ZnO Nanowires Arrays-Based Quantum Dot Sensitized Solar Cells. *Electrochim. Acta* **2013**, *99*, 204−210.

(22) Lou, Y.; Yuan, S.; Zhao, Y.; Hu, P.; Wang, Z.; Zhang, M.; Shi, L.; Li, D. A Simple Route for Decorating TiO_2 Nanoparticle over ZnO Aggregates Dye-Sensitized Solar Cell. *Chem. Eng. J.* **2013**, *229*, 190−196.

(23) Guo, M. Y.; Fung, M. K.; Fang, F.; Chen, X. Y.; Ng, A. M. C.; Djurišić, A. B.; Chan, W. K. ZnO and TiO_2 1D Nanostructures for Photocatalytic Applications. *J. Alloys Compd.* **2011**, *509*, 1328−1332.

(24) Yan, X.; Zou, C.; Gao, X.; Gao, W. ZnO/TiO_2 Core-Brush Nanostructure: Processing, Microstructure and Enhanced Photocatalytic Activity. *J. Mater. Chem.* **2012**, *22*, 5629−5640.

(25) Fan, J.; Zamani, R.; Fábrega, C.; Shavel, A.; Flox, C.; Ibáñez, M.; Andreu, T.; López, A. M.; Arbiol, J.; Morante, J. R.; Cabot, A. Solution-Growth and Optoelectronic Performance of ZnO:Cl/TiO_2 and ZnO:Cl/Zn_xTiO_y/TiO_2 Core−Shell Nanowires with Tunable Shell Thickness. *J. Phys. D: Appl. Phys.* **2012**, *45*, 415301.

(26) Mahajan, V.; Misra, M.; Raja, K.; Mohapatra, S. Self-Oorganized TiO_2 Nanotubular Arrays for Photoelectrochemical Hydrogen Generation: Effect of Crystallization and Defect Structures. *J. Phys. D: Appl. Phys.* **2008**, *41*, 125307.

(27) Mor, G. K.; Varghese, O. K.; Wilke, R. H. T.; Sharma, S.; Shankar, K.; Latempa, T. J.; Choi, K.-S.; Grimes, C. A. p-Type Cu−Ti−O Nanotube Arrays and Their Use in Self-Biased Heterojunction Photoelectrochemical Diodes for Hydrogen Generation. *Nano Lett.* **2008**, *8*, 1906−1911.

(28) Pradhan, D.; Mohapatra, S. K.; Tymen, S.; Misra, M.; Leung, K. T. Morphology-Controlled ZnO Nanomaterials for Enhanced Photoelectrochemical Performance. *Mater. Express* **2011**, *1*, 59−67.

(29) Hernández, S.; Cauda, V.; Hidalgo, D.; Farías Rivera, V.; Manfredi, D.; Chiodoni, A.; C. Pirri, F. Fast and Low-Cost Synthesis of 1D ZnO−TiO_2 Core−Shell Nanoarrays: Characterization and Enhanced Photo-Electrochemical Performance for Water Splitting. *J. Alloys Compd.* **2014**, DOI: 10.1016/j.jallcom.2014.02.010.

(30) Lamberti, A.; Sacco, A.; Bianco, S.; Manfredi, D.; Cappelluti, F.; Hernandez, S.; Quaglio, M.; Pirri, C. F. Charge Transport Improvement Employing TiO_2 Nanotube Arrays as Front-Side Illuminated Dye-Sensitized Solar Cell Photoanodes. *Phys. Chem. Chem. Phys.* **2013**, *15*, 2596−2602.

(31) Podrezova, L. V.; Porro, S.; Cauda, V.; Fontana, M.; Cicero, G. Comparison Between ZnO Nanowires Grown by Chemical Vapor Deposition and Hydrothermal Synthesis. *Appl. Phys. A: Mater. Sci. Process.* **2013**, *113*, 1−10.

(32) Rivera, V. F.; Auras, F.; Motto, P.; Stassi, S.; Canavese, G.; Celasco, E.; Bein, T.; Onida, B.; Cauda, V. Length-Dependent Charge Generation from Vertical Arrays of High-Aspect-Ratio ZnO Nanowires. *Chem.—Eur. J.* **2013**, *19*, 14665−14674.

(33) Chen, Y.; Stathatos, E.; Dionysiou, D. D. Microstructure Characterization and Photocatalytic Activity of Mesoporous TiO_2 Films with Ultrafine Anatase Nanocrystallites. *Surf. Coat. Technol.* **2008**, *202*, 1944−1950.

(34) Powell, C. J. Elemental Binding Energies for X-Ray Photoelectron Sspectroscopy. *Appl. Surf. Sci.* **1995**, *89*, 141−149.

(35) Pinna, N. X-Ray Diffraction from Nanocrystals. In *Scattering Methods and the Properties of Polymer Materials;* Springer: Berlin and Heidelberg, Germany, 2005; Chapter 4, pp 29−32.

(36) Toyoura, K.; Tsujimura, H.; Goto, T.; Hachiya, K.; Hagiwara, R.; Ito, Y. Optical Properties of Zinc Nitride Formed by Molten Salt Electrochemical Process. *Thin Solid Films* **2005**, *492*, 88−92.

(37) Hoang, S.; Guo, S.; Hahn, N. T.; Bard, A. J.; Mullins, C. B. Visible Light Driven Photoelectrochemical Water Oxidation on Nitrogen-Modified TiO_2 Nanowires. *Nano Lett.* **2011**, *12*, 26−32.

(38) Chen, D.; Jiang, Z.; Geng, J.; Wang, Q.; Yang, D. Carbon and Nitrogen Co-Doped TiO_2 with Enhanced Visible-Light Photocatalytic Activity. *Ind. Eng. Chem. Res.* **2007**, *46*, 2741−2746.

(39) Zhang, X.; Qin, J.; Xue, Y.; Yu, P.; Zhang, B.; Wang, L.; Liu, R. Effect of Aspect Ratio and Surface Defects on the Photocatalytic Activity of ZnO Nanorods. *Sci. Rep.* **2014**, *4*, Article number: 4596.

(40) Fragala, M. E.; Cacciotti, I.; Aleeva, Y.; Lo Nigro, R.; Bianco, A.; Malandrino, G.; Spinella, C.; Pezzotti, G.; Gusmano, G. Core−Shell Zn-Doped TiO_2−ZnO Nanofibers Fabricated via a Combination of Electrospinning and Metal−Organic Chemical Vapour Deposition. *CrystEngComm* **2010**, *12*, 3858−3865.

(41) Liao, D. L.; Badour, C. A.; Liao, B. Q. Preparation of Nanosized TiO_2/ZnO Composite Catalyst and its Photocatalytic Activity for Degradation of Methyl Orange. *J. Photochem. Photobiol., A* **2008**, *194*, 11−19.

(42) Madhusudan Reddy, K.; Manorama, S. V.; Ramachandra Reddy, A. Bandgap Studies on Anatase Titanium Dioxide Nanoparticles. *Mater. Chem. Phys.* **2003**, *78*, 239−245.

(43) Segura, A.; Sans, J. A.; Manjón, F. J.; Muñoz, A.; Herrera-Cabrera, M. J. Optical Properties and Electronic Structure of Rock-Salt ZnO under Pressure. *Appl. Phys. Lett.* **2003**, *83*, 278−280.

(44) Tanemura, S.; Miao, L.; Jin, P.; Kaneko, K.; Terai, A.; Nabatova-Gabain, N. Optical Properties of Polycrystalline and Epitaxial Anatase and Rutile TiO_2 Thin Films by RF Magnetron Sputtering. *Appl. Surf. Sci.* **2003**, *212*−*213*, 654−660.

(45) Morris, D.; Dou, Y.; Rebane, J.; Mitchell, C. E. J.; Egdell, R. G.; Law, D. S. L.; Vittadini, A.; Casarin, M. Photoemission and STM Study of the Electronic Structure of Nb-Doped TiO_2. *Phys. Rev. B* **2000**, *61*, 13445−13457.

(46) Dutta, S.; Chattopadhyay, S.; Jana, D.; Banerjee, A.; Manik, S.; Pradhan, S. K.; Sutradhar, M.; Sarkar, A. Annealing Effect on Nano-ZnO Powder studied from Positron Lifetime and Optical Absorption Spectroscopy. *J. Appl. Phys.* **2006**, *100*, 114328.

(47) Rajeshwar, K. Fundamentals of Semiconductor Electrochemistry and Photoelectrochemistry. In *Encyclopedia of Electrochemistry;* Wiley: Hoboken, NJ, 2002; Vol. *6*, p 608.

(48) Liu, J.; Chen, F. Plasmon-Enhanced Photoelectrochemical Activity of Ag−Cu Nanoparticles on TiO_2/Ti Substrates. *Int. J. Electrochem. Sci.* **2012**, *7*, 9560−9572.

(49) Mora-Seró, I.; Fabregat-Santiago, F.; Denier, B.; Bisquert, J.; Tena-Zaera, R.; Elias, J.; Lévy-Clément, C. Determination of Carrier Density of ZnO Nanowires by Eelectrochemical Techniques. *Appl. Phys. Lett.* **2006**, *89*, 203117−203117−3.

(50) Wang, G.; Wang, H.; Ling, Y.; Tang, Y.; Yang, X.; Fitzmorris, R. C.; Wang, C.; Zhang, J. Z.; Li, Y. Hydrogen-Treated TiO_2 Nanowire Arrays for Photoelectrochemical Water Splitting. *Nano Lett.* **2011**, *11*, 3026−3033.

(51) Hsu, C.-H.; Chen, D.-H. Photoresponse and Stability Improvement of ZnO Nanorod Array Thin Ffilm as a Single Layer of Photoelectrode for Photoelectrochemical Water Splitting. *Int. J. Hydrogen Energy* **2011**, *36*, 15538−15547.

(52) Yeh, M.-H.; Lin, L.-Y.; Chou, C.-Y.; Lee, C.-P.; Chuang, H.-M.; Vittal, R.; Ho, K.-C. Preparing Core−Shell Structure of ZnO@TiO_2 Nanowires Through a Simple Dipping−Rinse−Hydrolyzation Process as the Photoanode for Dye-Sensitized Solar Cells. *Nano Energy* **2013**, *2*, 609−621.

(53) Fabregat-Santiago, F.; Garcia-Belmonte, G.; Bisquert, J.; Zaban, A.; Salvador, P. Decoupling of Transport, Charge Storage, and Interfacial Charge Transfer in the Nanocrystalline TiO_2/Electrolyte System by Impedance Methods. *J. Phys. Chem. B* **2001**, *106*, 334−339.

(54) Laurenti, M.; Cauda, V.; Gazia, R.; Fontana, M.; Rivera, V. F.; Bianco, S.; Canavese, G. Wettability Control on ZnO Nanowires Driven by Seed Layer Properties. *Eur. J. Inorg. Chem.* **2013**, *2013*, 2520−2527.

(55) Choudhary, S.; Upadhyay, S.; Kumar, P.; Singh, N.; Satsangi, V. R.; Shrivastav, R.; Dass, S. Nanostructured Bilayered Thin Films in Photoelectrochemical Water Splitting—A Review. *Int. J. Hydrogen Energy* **2012**, *37*, 18713−18730.

(56) Parmar, K. P. S.; Kang, H. J.; Bist, A.; Dua, P.; Jang, J. S.; Lee, J. S. Photocatalytic and Photoelectrochemical Water Oxidation over Metal-Doped Monoclinic BiVO4 Photoanodes. *ChemSusChem* **2012**, *5*, 1926−1934.

(57) Su, J.; Guo, L.; Bao, N.; Grimes, C. A. Nanostructured WO_3/$BiVO_4$ Heterojunction Films for Efficient Photoelectrochemical Water Splitting. *Nano Lett.* **2011**, *11*, 1928−1933.